Author(s): Olley, Pete and Wagner, M.H.

Title: A modification of the convective constraint release mechanism in the molecular stress function model giving enhanced vortex growth

Publication year: 2006

Journal title: Journal of Non-Newtonian Fluid Mechanics

ISSN number: 0377- 0257

Publisher: Elsevier

Publisher's site: *http://www.sciencedirect.com*

Link to original published version: *http://dx.doi.org/10.1016/j.jnnfm.2006.01.002*

A modification of the convective constraint release mechanism in the molecular stress function model giving enhanced vortex growth

P. Olley [a*], M. H. Wagner [b]

[a] *School of Engineering, Design and Technology/ IRC in Polymer Engineering, EDT4, Chesham Building, University of Bradford, Bradford, BD7 1DP, UK.*
[b] *Polymertechnik/Polymerphysik, Technische Universität Berlin, Fasanenstrasse 90, D-10623 Berlin, Germany.*

Abstract
The molecular stress function model with convective constraint release (MSF with CCR) constitutive model [J. Rheol. 45 (2001), 1387] is capable of fitting all viscometric data for IUPAC LDPE, with only two adjustable parameters (with difference found only on reported "steady-state" elongational viscosities). The full MSF with CCR model is implemented in a backwards particle-tracking implementation, using an adaptive method for the computation of relative stretch that reduces simulation time many-fold, with insignificant loss of accuracy. The model is shown to give improved results over earlier versions of the MSF (without CCR) when compared to well-known experimental data from White and Kondo [J. non-Newt. Fluid Mech., 3 (1977), 41]; but still to under-predict contraction flow opening angles. The discrepancy is traced to the interaction between the rotational dissipative function and the large stretch levels caused by the contraction flow. A modified combination of dissipative functions in the constraint release mechanism is proposed, which aims to reduce this interaction to allow greater strain hardening in a mixed flow. The modified constraint release mechanism is shown to fit viscometric rheological data equally well, but to give opening angles in the complex contraction flow that are much closer to the experimental data from White and Kondo. It is shown (we believe for the first time) that a constitutive model demonstrates an accurate fit to all planar elongational, uniaxial elongational and shear viscometric data, with a simultaneous agreement with this well-known experimental opening angle data. The sensitivity of results to inaccuracies caused by representing the components of the deformation gradient tensor to finite precision is examined; results are found to be insensitive to even large reductions in the precision used for the representation of components. It is shown that two models that give identical response in elongational flow, and a very similar fit to available shear data, give significantly different results in flows containing a mix of deformation modes. The implication for constitutive models is that evaluation against mixed deformation mode flow data is desirable in addition to evaluation against viscometric measurements.

keywords: Molecular stress function; Simulation; Convective constraint release; Vortex growth; Opening angle

1. Introduction

Viscoelastic rheological modelling has steadily advanced in recent years. The 'separable' KBKZ model of Wagner [1] has had success in modelling much, but not all, rheological data. Using the damping function of Papanastasiou et. al. [2], the model was shown to fit rheological LDPE data in steady-state shear, uniaxial elongation, and first normal stress-difference. With the same parameters the model also gave a good fit to experimentally measured vortex opening angles measurements

* *+44 1274 234 537*
E-mail p.olley@bradford.ac.uk

in a 5.75:1 contraction ratio axisymmetric die [3]. Variations of the model could give non-zero second normal stress differences [4], and the model had considerable success in axisymmetric flows of strain-hardening polymer melt. The salient weakness of the model was its failure to give strain-hardening in planar elongation, with simultaneous shear softening; this lead to a general failure to predict vortex growth in planar contraction flows. A modification to the damping function permitted strain hardening in uniaxial, planar, and biaxial elongation, with simultaneous shear softening [5]. Simulation of strain-hardening LDPE flows using this model gave vortex growth in both axisymmetric and planar contraction flows [5, 6], however the model had the weakness that the rate of strain-hardening was below that seen in experiment [5].

A molecularly based model, the Molecular Stress Function (MSF) model was demonstrated to fit transient planar, uniaxial, and biaxial elongational data for long chain branched polymers, and to fit both first and second normal stress difference measurements in flows of un-branched polymer [7-10]. This was achieved with only a single adjustable parameter, originally used in a "fit-function", that related relative deformation to tube-stretch. The particular model given in [10] gave very significant improvement in vortex prediction, over earlier KBKZ models [11], but the model over-predicted shear stress and first normal stress difference in strain hardening melts [12].

More recent developments of the MSF model have focussed on a convective constraint release (CCR) mechanism, as first introduced by Marrucci [13]. This model uses a differential equation for tube stretch, originating from an energy-balance analysis, and employs two adjustable parameters. The model has been demonstrated to fit not only elongational data, but also shear stress and first and second normal stress difference for strain hardening melts. This model is the focus of this work, and is detailed in section 2.

Molecular considerations have figured strongly in other recent developments in rheological modelling - including the time-integral Pom-Pom model [14,15,16], the Double Convection Reptation model (DCR) (with both time-integral and differential forms) [17, 18, 19], and in differential models [20, 21]. Simulation of time-integral viscoelastic flows with particle tracking has been advanced by the work of Dupont and Crochet [3], Tanner [22,4] and Mitsoulis [23,24]. Techniques for tracking, solution, and tensor computation have been further developed [5, 11, 25]. A purely Eulerian approach, whereby the deformation fields are convected was introduced by Peters et. al [26], giving time-dependant two dimensional solutions. Rasmussen introduced a Lagrangian mesh method suitable for three dimensional time-dependant viscoelastic flows, including a Rivlin-Sawyers model [27], and a modified MSF with convective constraint release which was applied to membrane inflation [28].

It has not been shown that a time-integral constitutive model can fit all viscometric rheological data for IUPAC LDPE, and also match the vortex opening angle data in a 5.75:1 axisymmetric contraction flow measured by experiment by White and Kondo [29]. Concurring with such experimental data is an important requirement for a constitutive model, since it tests a model's response in a non-viscometric flow, containing a mixture of elongation and shear. This problem is studied in this work, and leads to a suggested modification to the convective constraint release mechanism

that further isolates elongational stretch from dissipation by shear. The resulting MSF model is shown to match the viscometric rheological data, and agree much more closely with the contraction flow experimental data.

2. The Molecular Stress Function model

The Molecular Stress Function model (MSF) gives the extra-stress in a flow, $\boldsymbol{\tau}(t)$, according to the time-integral model:

$$\boldsymbol{\tau}(t) = \int_{-\infty}^{t} m(t,t')\mathbf{S}_{\mathbf{MSF}}(t,t')dt' \ , \tag{1}$$

where $m(t,t')$ is a memory function between time t' in the past, and the current time t, and $\mathbf{S}_{\mathbf{MSF}}(t,t')$ is the strain measure between times t' and t. This strain measure can be written as:

$$\mathbf{S}_{\mathbf{MSF}}(t,t') = f^2(t,t')\mathbf{S}_{\mathbf{DE}}(t,t'), \tag{2}$$

where $\mathbf{S}_{\mathbf{DE}}(t,t')$ is the Doi-Edwards strain tensor [9, 10], and $f(t,t')$ represents the ratio of tube diameters a_0/a, where a is the tube diameter at time t, and a_0 is the tube diameter of the unstretched segments that were created at time t'.

Considerable progress was made by defining $f^2(t,t')$ as a function of the average value of the logarithm of the deformed tube segment lengths, $\langle \ln u' \rangle$, as defined in reference [10]. The strain energy of the system, W_{MSF} is proportional to $f^2 - 1$; introduction of a maximum value for stored energy, and thus stretch, led to a fit-function for $f^2(t,t')$ in terms of only $\langle \ln u' \rangle$ and a single parameter. The model was shown capable of fitting a wide range of transient and steady state measurements in elongational flows for a range of polymer melts [9, 10]. An additional attraction is that simulations with this model can be performed using the computationally efficient "backwards integration" method employed for KBKZ type models [11]. Despite the quantitative accuracy for elongational flows, there remained a degree of over-prediction of shear stress and first normal stress difference in shear flow [12].

Physical consideration of the rate of storage of energy, and the rate of dissipation of energy lead to an evolution equation for f^2 of the form:

$$\frac{\partial f^2}{\partial t} = \frac{\beta f^2}{1 + \frac{\beta - 1}{f^4}} \left(\mathbf{k} : \mathbf{S} - \frac{1}{f^2 - 1} CR \right), \tag{3}$$

where **k** is the velocity gradient tensor, **S** is the orientation tensor (where **S** = 1/5 $\mathbf{S}_{\mathbf{DE}}$). The parameter β is equal to unity for linear melts, and (normally) equal to 2 for strain hardening melts [12, 30, 31]. The term CR is a form of the convective constraint release mechanism suggested by Marrucci [13].

2.1 Convective constraint release in the Molecular stress function.

The form of the convective constraint release mechanism, CR, was established in ref. [12] as:

$$CR = \left(f^2 - 1\right)^2 g\left(\mathbf{q}, \overline{\mathbf{q}}, \overline{\mathbf{p}}\right), \tag{4}$$

where $\mathbf{q}, \overline{\mathbf{q}}$ and $\overline{\mathbf{p}}$ are the unit vector normal to tube cross-section, its affine time derivative, and the affine time-derivative of a unit vector tangential to a tube, respectively [12]. It was shown that $\overline{\mathbf{q}}$ and $\overline{\mathbf{p}}$ are always coaxial in non-rotational flow, and always perpendicular in shear flow. This led to $g\left(\mathbf{q}, \overline{\mathbf{q}}, \overline{\mathbf{p}}\right)$ being expressed in terms of two dissipative functions $g_1\left(\mathbf{q}, \overline{\mathbf{q}}, \overline{\mathbf{p}}\right)$, and $g_2\left(\mathbf{q}, \overline{\mathbf{q}}, \overline{\mathbf{p}}\right)$ which respond very differently to rotational and irrotational flows.

The linear addition of these two functions has been used by Wagner as the "simplest" continuation, giving a constraint release mechanism with two parameters, a_1 and a_2 :

$$CR = \frac{1}{2}\left(f^2 - 1\right)^2 \left[\, a_1 g_1\left(\mathbf{q}, \overline{\mathbf{q}}, \overline{\mathbf{p}}\right) + a_2 g_2\left(\mathbf{q}, \overline{\mathbf{q}}, \overline{\mathbf{p}}\right) \,\right] \tag{5}$$

For flows involving changes in deformation rate, these two functions can be expressed objectively in terms of the orientation tensor, $\mathbf{S}$, and the Rivlin-Ericksen tensors , $\mathbf{A_1}$ and $\mathbf{A_2}$ [12]:

$$g_1\left(\mathbf{q}, \overline{\mathbf{q}}, \overline{\mathbf{p}}\right) = g_1\left(\mathbf{S}, \mathbf{A_1}\right) = \frac{1}{2}\sqrt{\mathbf{A_1^2 : S}}\,, \tag{6}$$

and

$$g_2\left(\mathbf{q}, \overline{\mathbf{q}}, \overline{\mathbf{p}}\right) = g_2\left(\mathbf{S}, \mathbf{A_1}, \mathbf{A_2}\right) = \frac{1}{2}\sqrt{\left|\mathbf{A_2 : S - A_1^2 : S}\right|}\,. \tag{7}$$

The two Rivlin-Ericksen tensors are given by

$$\mathbf{A_1^2} = 4\mathbf{D^2}\,, \tag{8}$$

and

$$\mathbf{A_2} = \frac{D\mathbf{A_1}}{Dt} + \mathbf{A_1^2} + 2\left(\mathbf{W}\cdot\mathbf{D} + \mathbf{D}\cdot\mathbf{W^T}\right), \tag{9}$$

where **W** and **D** are the rate of rotation tensor, and rate of deformation tensor respectively, given by:

$$\mathbf{W} = \frac{1}{2}\left(\mathbf{k} - \mathbf{k^T}\right), \tag{10}$$

and

$$\mathbf{D} = \frac{1}{2}\left(\mathbf{k} + \mathbf{k^T}\right). \tag{11}$$

The function $g_1\left(\mathbf{S}, \mathbf{A_1}\right)$ is significant in elongational flows, whereas $g_2\left(\mathbf{S}, \mathbf{A_1}, \mathbf{A_2}\right)$ is significant in rotational flow. Crucially, $g_2\left(\mathbf{S}, \mathbf{A_1}, \mathbf{A_2}\right)$=0 in constant strain-rate extensional flows; this allows CR to distinguish between rotational and irrotational flows [12].

The current work assesses the models performance against experimental data for LDPE in a 5.75 : 1 axisymmetric contraction flow from White and Kondo. It is noted that in the complex flows encountered in the geometry ('complex' implying a combination of shear and elongation, that varies along a particles path), the rise in $f^2(t,t')$ is much lower than that given by earlier MSF models (without CCR), and achieves both lower stress levels and vortex growth than expected. We reason that the large values of f^2 induced by the elongational flow into the contraction suffer heavy dissipation from the $g_2(\mathbf{S}, \mathbf{A_1}, \mathbf{A_2})$ term, due to the levels of shear, and rate change, in the flow. Examination of the evolution equation for f^2 shows that the dissipation rate of f^2 due to rotational flow is approximately proportional to $f^4 g_2(\mathbf{S}, \mathbf{A_1}, \mathbf{A_2})$ at large f; this gives a very large rate of dissipation in the contraction since f^2 is typically an order of magnitude higher than values reached in simple shear flow.

We propose a method to isolate stored elongational energy from heavy dissipation by modest rotational components; we make the dissipation rate for f^2 relatively independent of the magnitude of f, whilst maintaining the behaviour of the original at low values of f, especially the asymptotic nature around $f^2 = 1$.

$$CR = \frac{1}{2}\left(f^2 - 1\right)^2 \left[\; a_1 g_1(\mathbf{S}, \mathbf{A_1}) + a_2 \frac{g_2(\mathbf{S}, \mathbf{A_1}, \mathbf{A_2})}{f^4} \; \right] \qquad (12)$$

The method does not change the behaviour in constant rate elongational flow, since function g_2 is then zero. In the remainder of this work, we refer to the evolution equation, Eq.3, with the original linear combination of functions g_1 and g_2 given in Eq.5 as 'model CR1', and with the weighted combination expressed in Eq.12 as 'model CR2'.

2.2 Comparison with rheometric data

We assess the models against flows of the IUPAC LDPE melt. This is because the melt is particularly well characterised with memory function data, and sufficient transient and steady-state rheometric data to give a "best fit", with enough data for independent cross-comparison between transient and steady-state predictions. Experimental results are available for an abrupt 5.75:1 contraction ratio die, allowing direct comparison with simulation. Throughout this work, we assume that the memory function in Eq.1 can be approximated by the well known sum of exponentials:

$$m(t,t') = \sum_i \frac{g_i}{\lambda_i} \exp\left(-\frac{(t-t')}{\lambda_i} \right). \qquad (13)$$

We use the relaxation times, λ_i , and relaxation moduli, g_i , data from Laun [32, 33]. The relaxation times and moduli at the different temperatures relevant to IUPAC LDPE data are tabulated in ref. [11]. A value of β=2 was appropriate for the strain-hardening rate of the material, this value is used throughout this work.

Figure 1 shows the response of f^2 from models CR1 and CR2 in elongational and shear flow. Values of a_1 were obtained from best fit to the transient planar and uniaxial elongation data at 125°C from Laun and Schuch [34], then values of a_2 were obtained by fitting to the steady state shear data from Meissner [35]. Both models use the same value of a_1 ($a_1 = 0.012$), but different values of a_2 ($a_2 = 0.07$ for model CR1, and $a_2 = 0.55$ for model CR2).

As shown in [12], f^2 rises to a plateau in elongational flow with model CR1, whereas in shear flow it rises to a peak (a few units high) and then reduces back to unity; elongational behaviour is identical using model CR2 (since $g_2 = 0$). Qualitative behaviour in shear is the same with a peak followed by a reduction to unity. The peak is seen to be shifted to a slightly higher strain (due to the greater dissipation at low f^2), this peak is followed by a sharper fall.

We note first that model CR1 gives an excellent fit to the key IUPAC rheometric data using a_1 =0.012, and a_2 =0.07 : data for steady-state shear, steady-state first normal stress difference, transient planar elongation, transient uniaxial elongation and transient shear are all fitted simultaneously by this one model. This is clearly a very significant advance over previous models, including the MSF without CCR (which over predicted stresses in shear [12]), and the 'adapted KBKZ' model [5] (which additionally gives a slower rise rate than transient elongational data).

We demonstrate the (equally accurate) viscometric response of the variation 'model CR2' in Figures 2 and 3. Figure 2 compares the fit of models CR1 and CR2 in comparison to the transient elongational and shear data from Laun and Schuch at 125°C [34]. Both planar and uniaxial elongational data are well fitted, and the rate, slight overshoot, and large strain asymptote of shear viscosity are closely matched by both models. The fit to the transient shear data is effectively a prediction of the models from choosing their respective values of a_2 to fit Meissner's steady-state shear data at 150°C.

Figure 3 compares steady-state shear predictions of model CR1 and CR2 with Meissner's data [35]. For completeness predictions for steady-state elongational viscosity are compared with uniaxial measurements reported in ref. [33]. Using a_2 = 0.07 for CR1, and a_2 = 0.55 for CR2, both models give an excellent fit to both shear stresses and first normal stress difference, without a tendency for over-prediction.

3. Time-integral simulation method

From a computational point of view, the 'MSF with CCR' model differs greatly from MSF models without CCR, and 'traditional' KBKZ models. The single greatest difference is that the stress integration cannot be performed monotonically as one tracks a particle backwards in time. The reason for this is that to find the stress contribution from a time t' in the past, one must know not only the Doi-Edwards tensor between times t' and the current time, t, but also the relative stretch between times t' and t, $f^2(t,t')$. This involves starting with an isotropic distribution for **S** at time t' and f^2=1 (i.e. $f^2(t',t') = 1$), and integrating f^2 forwards in time through all

times t'', where $t' \le t'' \le t$. It is perhaps of value to state that the terms $\mathbf{S}$ and f^2, as they appear in Eq.3, are $\mathbf{S}(t'',t')$ and $f^2(t'',t')$, respectively.

3.1 Overview of the solution method

The simulation uses nine-noded bi-quadratic elements to represent velocity components, with one order lower interpolation used for pressure. An initial Stokes' flow solution is computed to start the iterative process. The viscoelastic stress resulting from the flow solution of the previous iteration is computed for each Gauss point in each element; to obtain the stress for a particle at a Gauss point it is necessary to know the history of that particle. The flow kinematics are used to track a particle 'backwards' in time, the method used for tracking is given in detail in ref [11]; this reference details the streamline tracking method, and the method for locating the particle's position in an element's natural coordinate system as the particle is tracked back through many elements on its course.

3.2 History-storage and time-step considerations

The particle strictly needs to be tracked back to " - ∞", in practice this must be moderated – we use 5 times the longest relaxation time as the target. The velocity gradient tensor **k** is computed by the least-squares method, described in [23], to give a smooth and continuous velocity gradient field. As discussed in [5], the trace of **k,** resulting from an incompressible finite-element flow solution, will not in general be zero, thus the 'error' in the trace is 'shared' between the diagonal terms to maintain a physical meaningful deformation gradient tensor. The deformation gradient tensor, $\mathbf{F}(t,t')$ is computed by solution of

$$\frac{d\,\mathbf{F}(t,t')}{dt'} = \mathbf{k}(t')\mathbf{F}(t,t'). \qquad (14)$$

As detailed in ref. [11], a 4th order Runga-Kutta method, with controlled integration time steps was used to compute $\mathbf{F}(t,t')$; the combination will be shown (in section 4.3) to maintain unity determinant until a point that approaches the limit set by machine precision (64-bit). When, along some particle tracks, the deformation gradient tensor, $\mathbf{F}(t,t')$ starts to become ill-conditioned (we use $\left(\left|\det(\mathbf{F})-1\right| > 0.05\right)$ as the test), back tracking is stopped and the final value of $\mathbf{F}$ is used for earlier stress contributions; results will be shown insensitive to this (in the case that **F** is computed to a precision which approaches the expected limit with 64-bit computation).

Values that need to be stored at each time s, where $s = t - t'$, are: s, $\mathbf{F}^{-1}(t,t')$, $\mathbf{k}(t')$, and integration weights arising from the time-integration scheme to be used.

Time stepping considerations are slightly more involved than with KBKZ type models. As with KBKZ-type models, time steps need to be moderated to allow accurate integration of the exponential time-constant weights implied by the memory function approximation (Eq.13), and they also need to be moderated for accurate tracking through elements. For the MSF with CCR model, the accurate resolution of

the history of f^2 must be considered independently. Consideration of Eq.3 , and Eqs.5 and 12 suggests that significant errors in the resolution of f^2 are likely if there is a large change in the velocity gradient tensor **k**, or the orientation tensor **S** over a single time-step. To moderate this effect, the current rate of change of **k**, $\frac{d\mathbf{k}}{dt}$ was estimated from finite differencing the two latest samples of **k**. It was ensured that:

$$\Delta t \times \left|\frac{d\mathbf{k}}{dt}\right| \leq \frac{1}{10}|\mathbf{k}| \ , \tag{15}$$

where $|\mathbf{z}|$, implies the magnitude of a tensor, $\mathbf{z}$, given by $\sqrt{\frac{1}{2}\mathbf{z}:\mathbf{z}^{\mathbf{T}}}$. This additional limitation on the time-step limits changes in the velocity gradient tensor to around 10% per step to assist resolution. The additional requirement involves significant extra computation, but is very effective in picking up regions of high 'activity' in the distant past, and gives much better convergence if included than if omitted. We ascribe this to the reduced variation due to 'chance' sampling as particles flow past localised regions of high deformation rate, such as particles in both the main flow and the vortex that flow past the 'lip'.

3.3 Stress computation

To perform the stress integration in Eq.1 it is necessary to know the stretch between any time in the past, t', and the current time, t. To do this f^2 must be computed forwards in time according to Eq.3, starting at value 1 at time t' ($f^2(t',t')=1$) to arrive at the relative stretch $f^2(t,t')$. To achieve this the orientation tensor relative to time t', $\mathbf{S}(t'',t')$, must be determined for all intermediate times, t'', where $t \geq t'' \geq t'$; starting with an isotropic distribution at time t', and ending with $\mathbf{S}(t,t')$. The integration of f^2 moves thorough all intermediate times. For these computations it is appropriate to denote the stored values of (inverted) deformation gradient tensor and velocity gradient tensor that lie between times t' and t as $\mathbf{F}^{-1}(t,t'')$, and $\mathbf{k}(t'')$.

3.3.1 Computation of f^2

The deformation gradient tensor between time t' and time t'', $\mathbf{F}(t'',t')$, can be deduced from stored values using:

$$\mathbf{F}(t'',t') = \mathbf{F}(t,t')\mathbf{F}^{-1}(t,t''), \tag{16}$$

from the chain rule detailed by Tanner [22]. $\mathbf{F}(t'',t')$ can then be used to calculate the relative orientation tensor between t' and t'', $\mathbf{S}(t'',t')$ [12]. This can be done by direct spherical integration, as in ref. [11], or to a close approximation by calculating the Cauchy tensor, $\mathbf{C} = \mathbf{F}^{\mathbf{T}}\mathbf{F}$, the Finger strain tensor, $\mathbf{F}^{-1}\left(\mathbf{F}^{-1}\right)^{T}$, and then using Currie's approximation [36]. In view of the very large number of times that the relative orientation tensor **S** must be calculated to compute f^2, and its significant

computational cost when done by numerical integration, we use Currie's approximation throughout in simulations.
With $\mathbf{S}(t'',t')$, $\mathbf{k}(t'')$, and time s available at all storage points, the rate of rotation, and rate of deformation tensors $\mathbf{W}(t'')$, and $\mathbf{D}(t'')$ can be deduced using Eqs.10 and 11, and the rate of change of the Rivlin-Eriksen tensor $d\,\mathbf{A_1}/d\,t$ can be calculated. We compute the time derivative of $\mathbf{A_1}$ by finite-differencing in time between the value of $\mathbf{A_1}$ at time t' and the value of $\mathbf{A_1}$ at previous point *backtracked* to (i.e. at $t'+\Delta t'$). This gives a value for the derivative that is a representative average between these two times, this is consistent with the forward integration used to calculate f^2. It will be appreciated that (much) repeated computation can be saved by storing these three derived tensors whilst tracking the particles history.

The dissipation functions g_1 and g_2 can now be computed from Eqs.6-9, and Eq.3 can be integrated over any time t'', allowing $f^2(t,t')$ to be calculated. We employ an adaptive fourth order Runga-Kutta method to integrate Eq.3.

3.3.2 Adaptive computation point selection

The direct computation of $f^2(t,t')$ for every point indicated by the time-stepping criteria can be prohibitively slow. We use an adaptive method whereby $f^2(t,t')$ is computed for a number of values of t', with linear interpolation over the interval between these values; it is first checked (by a computationally inexpensive method) that linear interpolation is accurate over an interval; if not then a new point is calculated between them by direct integration of Eq.3. This continues (recursively) until all intervals have been verified.

The process begins by selecting a number of values of t' for direct computation of $f^2(t,t')$. We select values closest to each the time constants, λ_i, in the memory function, and also the values closest to $2\times\lambda_i$, and $5\times\lambda_i$ to give an approximately even spread in a logarithmic sense (assuming there is a factor of 10 between adjacent λ_i). The points representing the largest value of s recorded during 'backtracking', and the point representing $t'=t$ must also be selected to give full coverage for interpolation. For the memory function data used, with 8 relaxation times from $\sim 10^{-4}$ to $\sim 10^{3}$ this gives an initial spread of around 25 'seed' points, t_0, t_1, t_2, t_3, .. as shown in Figure 4.

To make checking computationally inexpensive, the adaptive method checks the interpolation across an interval by evaluating linear interpolation across *two* intervals; this interpolation can be compared with the point in between that has already been computed by direct integration. Initially the interval between t_0 and t_1 is checked: the values of $f^2(t,t_0)$ and $f^2(t,t_2)$ are used in linear interpolation to give an estimated value of $f^2(t,t_1)$, which we write as $\hat{f}^2(t,t_1)$. If it is found that:

$$\left|\hat{f}^2(t,t_1)-f^2(t,t_1)\right|\le\varepsilon\,, \qquad (17)$$

where ε is the permitted error, then the interval t_0 to t_1 is deemed resolved by linear interpolation, and checking proceeds to the next interval (t_1 to t_2). If the criterion is not met, then a new point, t_{1a} is deemed necessary between t_0 and t_1; the nearest storage point to the mid-point is used. The value of $f^2(t,t_{1a})$ is then calculated by direct integration, and the checking proceeds to checking the interval between t_0 and t_{1a}. This continues recursively until all intervals between direct integration points have been verified.

The final interpolation is, of course, performed using adjacent values. For the contraction flows studied, a value of 0.05 for ε was found to give insignificant difference in computed stresses, compared with stresses computed using every point. This strategy of checking by interpolation across two existing intervals avoids additional (expensive) direct computations of f^2, unless shown necessary. The efficiency of the adaptive method is suggested by the variation in the number of points added in simulation. In contraction flow, the method typically adds an average of around 100 direct integration points; many fewer (~10-40) for particles wholly in the 'quiet' upstream region, and many more (~300-3000) for particles passing the lip, or in the vortex. The adaptive method reduces our overall simulation time by a factor of over 20, compared with direct integration at every point.

3.3.3 Stress integration

With the value of $f^2(t,t')$ available at each stored point (by linear interpolation unless directly computed), there remains only the computation of $\mathbf{S}_{\mathbf{DE}}(t,t')$. This is straightforward as $\mathbf{F}^{-1}(t,t')$ is stored for all points, and Currie's approximation can be used as outlined in section 3.3.1. The time-integration of Eq.1 may then be performed using the Gauss-Legendre derived weights that were stored during 'backtracking'.

3.4 Updating the flow fields

The velocity and pressure field update scheme we use is based upon that of Viriyayuthakon and Caswell [37]. The method we use here contains a small, but valuable, modification to the method detailed in ref [5]. For context, we summarise the method given in [5].

For an assumed steady-state flow, with negligible inertia and body-forces, we require:

$$\nabla\cdot\left(\boldsymbol{\tau}_{\mathbf{v}}-\mathbf{I}p\right)=0\,, \tag{18}$$

where $\boldsymbol{\tau}_{\mathbf{v}}$ are the viscoelastic extra-stresses computed using Eq.1, and p is pressure. We add notional Newtonian stresses, $\mu\left(\mathbf{k}+\mathbf{k}^{\mathbf{T}}\right)$ to each side of the equation, and rearrange to give:

$$\left[-\nabla\cdot\left(\mu\left(\mathbf{k}+\mathbf{k}^{\mathbf{T}}\right)-\mathbf{I}p\right)\right]_{N+1}=\left[\nabla\cdot\left(\boldsymbol{\tau}_{\mathbf{v}}-\mu\left(\mathbf{k}+\mathbf{k}^{\mathbf{T}}\right)\right)\right]_{N}\,, \tag{19}$$

where the subscripts imply that the viscoelastic and Newtonian stresses from iteration N, are used to give a body force for the N+1th flow solution. The iterative procedure begins with an initial Newtonian flow solution, and proceeds until convergence is attained. The value of μ that is used is important, we use $\mu=\omega\mu_0$, where μ_0 is the

numerically predicted value of low shear viscosity, given by $\mu_0 = \sum \lambda_i g_i$, and ω is a scalar. Viscoelastic stresses can be much higher than notional Newtonian stresses given by the low shear viscosity, due to strain hardening and stress convection. If ω is too small, the resistance to change in the velocity field is insufficient (as the notional Newtonian stresses are too small compared with the viscoelastic stresses), and the possibility of good convergence is lost. If ω is too high, the rate of convergence is reduced, also the final level of convergence that is achieved is reduced (when the direct damping effect of ω on velocity is accounted for in the convergence measure).

Previously we have chosen a suitable value of ω for a flow-rate, and proceeded with one solution of Eq. 19 per stress computation; values of ω of up to 60 were needed at the highest flow rates for good convergence, and convergence can be very slow. A more efficient method is to use *m sub-iterations* of the flow solution method via:

$$\left[-\nabla\cdot\left(\mu\left(\mathbf{k}+\mathbf{k}^{\mathrm{T}}\right)-\mathbf{I}p\right)\right]_{k+1} = \left[\nabla\cdot\boldsymbol{\tau}_{\mathbf{v}}\right]_N - \mu\nabla\cdot\left[\left(\mathbf{k}+\mathbf{k}^{\mathrm{T}}\right)\right]_k \qquad (20)$$

where the subscripts imply that sub-iteration k gives the notional Newtonian stresses that are used to calculate the k+1th sub-iteration flow solution. Initially *m* is set equal to ω. The number of sub-iterations is maintained at *m* for a number of viscoelastic stress iterations until it is detected that further useful progress has ceased (see later); at this point *m* is halved (to nearest integer). These stepped decrements continue until *m* = 1.

The advantage of the procedure is much faster convergence rate. This appears to happen by allowing features which are usually slow to reach convergence (e.g. correction pressure) to progress quickly towards their approximate final values when *m* is large. More sensitive features such as vortex angle tend to oscillate (greatly) during this phase. As *m* falls, the oscillations in the more sensitive features fall to fine detail level. Oscillations in the 'outputs': vortex intensity, vortex angle, correction pressure, and vortex area were monitored by the code. The time to halve *m* was taken to be when *each* of these outputs had arrived at a value that had been 'crossed' three times during that value of *m* (indicating oscillation about the solution point). In most instances, the 'outputs' listed had settled to four significant figures in the simulations reported.

A minimum convergence of $\omega V_r < 2\times10^{-4}$ was obtained for all MSF with CCR simulations in this work (where V_{r} is the maximum change in any velocity component over a full viscoelastic stress iteration, N to N+1, (explicitly not over a sub-iteration) divided by the maximum flow velocity). Similarly the relative change in pressure was always better than 4×10^{-4}. Both of these convergence figures are significantly better than those obtained for the earlier fit-function MSF model [10] (by factors of 5 for velocity, and 20 for pressure). These comparisons have been checked using the same mesh, material, flow-rates, software, and time-stepping criteria and indicate that it is the MSF with CCR *model* that is giving better convergence. The most obvious differences in prediction between the MSF with CCR model and the earlier fit-function MSF model is that the earlier model gives high shear viscosity and

first normal stress difference, N1. This suggests that the lower shear predictions, given by the MSF with CCR, are resulting in improved convergence behaviour.

4. Simulation procedure

The MSF model with CCR was applied to a 5.75:1 axisymmetric contraction flow, and a 8:1 planar contraction flow. Experimental data for vortex opening angle is available for the former geometry [29]. Both the original constraint release formulation, 'MSF model CR1', and the modified formulation, 'MSF model CR2' were applied to the flows, along with the earlier fit-function MSF model [10], which we refer to as 'MSF without CCR', for comparison. Simulations were performed using relaxation data for 160°C; solutions were obtained at apparent shear rates of 0.125 s^{-1}, 0.25s^{-}1, 0.5s^{-1} , ... continuing in factors of two whilst convergence was satisfactory. A convergence value of $\omega V_r < 1\times10^{-3}$ was required for the 'MSF without CCR' model; the convergence of the CCR models was found to be significantly better allowing the tighter requirement: $\omega V_r < 2\times10^{-4}$.

4.1 Application to 5.75:1 axisymmetric contraction flow

The models were used with rheological data and parameters for IUPAC LDPE at 160°C. White and Kondo made measurements for several brands of LDPE (including IUPAC) at several temperatures, and showed that all of these results formed a single curve, when plotted against the fully-developed downstream wall Stress Ratio. This ratio, Sr, is given by :

$$Sr = \frac{N1}{2\tau_w} \quad , \tag{21}$$

where N1 is the first normal stress difference at the wall, and τ_w is the shear stress at the wall.

The experimental results of White and Kondo are compared with the three models in Figure 5. MSF model CR2 is seen to show a strong rise in opening angle with Sr, and whilst there remains a difference in rise-rate, the strong growth is similar to the experimental data. The largest opening angle obtained is 51 degrees at a value of Sr of 2.3. MSF model CR1 falls well below the experimental data giving a peak of 32 degrees at Sr = 1.9. The fit-function MSF model, 'MSF without CCR', is notably 'late' when represented in this way. A peak of 44 degrees is obtained, but at Sr = 10.7. The 'lateness' may be attributed to the over-prediction of N1 in shear by this model, which gives over-prediction of Sr at a given wall shear rate. MSF model CR2 clearly gives the best quantitative and qualitative behaviour against this experimental data.

For interest, the vortex intensity given by the models is shown in Figure 6. The vortex intensity is defined as the ratio of the volumetric flow rate in the vortex, to the volumetric flow rate passing through the die. All three models show a peak at an apparent shear rate of around $10s^{-1}$, with CR2 giving a much stronger vortex than CR1. The 'MSF without CCR' is seen to be more similar to model CR2 when plotted against apparent shear rate. Figure 7 shows the contours of streamfunction for the three models at an apparent shear rate of $32s^{-1}$ (a rate at which model CR2 is very close to the experimental data). The contours in the vortexes are plotted at integer

multiples of 1% vortex intensity and show the generally stronger vortex behaviour of model CR2.

Figure 8 plots the entrance correction pressure for the three models. Model CR2 gives higher correction pressure than model CR1 as the flow rate rises, as might reasonably be expected as (as will be shown directly) it gives greater strain-hardening in 'mixed' elongational flow. Both curves are higher than that of the MSF without CCR model.

4.2 Application to 8:1 planar contraction flow

Experimentally, pronounced vortex growth with increasing flow rate is well established for planar contraction flows of LDPE, for example ref. [38] shows opening angles in excess of 50° at high flow rates. Figure 9 shows the opening angles obtained by simulation. Model CR1 rises to a peak of 34 degrees at an apparent shear rate of 256 s^{-1}, whereas model CR2 rise more strongly to a highest value of 47 degrees at the same rate. The 'MSF without CCR' model approximately follows the line of model CR2, until an apparent shear rate of 64s^{-1}, after which satisfactory convergence wasn't obtained. Figure 10 shows the contours of streamfunction for the three models at an apparent shear rate of 32 s^{-1}. Contours in the vortexes are plotted at integer multiples of 0.2% for these flows. Model CR2 gives the strongest vortex, but perhaps more significantly, it is the only model giving the pronounced vortex 'bulge' found in experimental visualisation experiments (see ref. [38]). The evolution of the vortex, with growing flow rate, can be seen in figure 11.

Figure 12 Shows the vortex intensity obtained using the three models. These follow a similar pattern to their axisymmetric counterparts, with increasing intensity obtained in the order CR1, 'MSF without CCR', and CR2. The peaks are lower, at 1.6% for CR2, and are at approximately four times the apparent shear rate compared with the 5.75:1 axisymmetric contraction. This suggests they occur at comparable levels of elongation rate in both geometries. Figure 13 gives the correction pressures for the flow. Again models CR1 and CR2 follow a similar path, with CR2 rising more steeply at high rates, as can be expected from the greater strain-hardening.

An important effect on stress of the three models is illustrated by Figure 14. This shows contours of the Principal Stress Difference (PSD) for the 8:1 planar contraction flow at an apparent shear rate of 32s^{-1}. Comparing models CR1 and CR2 reveals clearly higher stress levels (~30%) from CR2, despite their constant rate viscometric responses being difficult to separate. This demonstrates the effectiveness of model CR2 in isolating large values of f^2, that are induced by elongational flow, from heavy dissipation by rotational flow. Detailed examination of the centre-line stresses reveals them to differ by only a few percent. The flow along this line is irrotational, but it is not constant rate; as the rate changes then $d\mathbf{A}/dt$ is non-zero, and thus $g_2(\mathbf{S}, \mathbf{A_1}, \mathbf{A_2})$ is non-zero – giving a slight difference between CR1 and CR2 in this region. The 'MSF without CCR' model gives qualitatively different behaviour with greatly increased PSD near the downstream wall; the over-prediction of shear-stress and N1 with the model seems the clear explanation.

4.3 Effects of finite precision computation of the deformation gradient tensor

In the flows studied (characterised by an abrupt 'lip', high apparent shear rates, and a longest time constant of 701 seconds), very large deformations need to be represented by the deformation gradient tensor, **F**. In Appendix 1, we deduce a condition number, C, which gives the expected error in the determinant of **F** due to representing the components of **F** to finite precision. The expected error is shown in Appendix 1 to be of the order of

$$\frac{C}{10^N}, \tag{22}$$

where

$$C = \frac{1}{2}\left(\left|F_{rr}\, F_{xx}\, F_{\theta\theta}\right| + \left|F_{rx} F_{xr} F_{\theta\theta}\right| \right) \tag{23}$$

(for axisymmetric flow), and N is the number of decimal digits used in the computations. The current simulations were performed using 64-bit precision giving approximately 16 significant decimal figures, i.e. N≈16. From Eq. 22, the expected error in the determinant (due to rounding) is of order 1 for a condition number of 10^{16}. For a condition number of 10^{14}, an error in the determinant of order 10^{-2} is expected; this is the order of error in the determinant (5×10^{-2}) that is 'trapped' by the software and causes it to discontinue back-tracking for that particle. Discontinuing backtracking at a point is equivalent to neglecting the strain history of the particle that occurred *before* that point. The current simulation uses a high order integration scheme for the computation of **F** in conjunction with controlled integration time steps; also the trace of **k** is enforced to zero. Condition numbers of **F** were monitored in detail over a full-field stress computation for a particular flow (model CR2 in the 5.75:1 axisymmetric abrupt contraction flow, at an apparent shear rate of 64 s^{-1}); the minimum condition numbers when the situation $\left|\det(\mathbf{F})-1\right| > 0.05$ was encountered were $\sim10^{13}$, with a maximum observed of $\sim10^{14}$. Approximately equal numbers occurred in each 'decade' (in this section the notation "$\sim10^{n}$" is used to imply numbers greater or equal to 1×10^{n}, but less than $1\times10^{n+1}$). Since an error of order 10^{-2} is expected in the determinant of **F** at a condition number of 10^{14}, the accuracy of the computation of **F** in the simulations is seen to approach the expected limit for 64-bit representation.

Some numerical experiments were performed to investigate the sensitivity of results to the precision of representation of **F**, and its method of computation.

In the first experiment, the maximum time-step permitted for a single application of the Runga-Kutta integration of **F** (Δt_I) was reduced to $\Delta t_I\, g_{\max} \le 1/50$, where $g_{\max}$ is the largest eigenvalue of the velocity gradient tensor, **k** (the "standard" time-step was $\Delta t_I\, g_{\max} \le 1/5$). This change gave no clear change in the range of condition numbers achieved when $\left|\det(\mathbf{F})-1\right| > 0.05$ was encountered (minimum C of $\sim10^{13}$, maximum C of $\sim10^{14}$, with approximately equal numbers in each decade).

In the second experiment, **F** was computed using the "standard" time-step, but a method was applied to 'force' **F** to have unity determinant after each time step (detailed in Appendix 2), for as long as available precision permitted. This method

increased the range slightly, with the minimum C of $\sim 10^{14}$, and a maximum C of $\sim 10^{15}$; the majority occurred at $\sim 10^{14}$.

In the third experiment, **F** was computed to 32-bit precision representation (to be precise **F** was computed using the 64-bit method, but after each time-step the components of **F** were reduced to 32-bit precision). On the machine used for simulation, 32-bit precision gives approximately 7 significant decimal figures ($N \approx 7$). With this method the minimum value that the condition numbers reached when $|\det(\mathbf{F}) - 1| > 0.05$ was $\sim 10^4$, with a maximum of $\sim 10^5$; again these are consistent with the predictions of Eq. 22.

The results for vortex intensity, opening angle, and correction pressure from the experiments are summarised in Table 1. Opening angles are the 'automated' opening angles detailed in ref. [5], these are slightly below the true (tangential) opening angles (by approximately 1/2 degree at $64s^{-1}$), but are measured by the software to high precision to show any variation.

The results demonstrate considerable robustness, with negligible variation to the graphical scales of Figures 5, 6, and 8. With 32-bit precision, the computation of **F** was discontinued at values of C of only $\sim 10^4$ to $\sim 10^5$, even with this drop in precision, the results vary very little (the levels of convergence that were obtained were reduced by a factor of over 2, a major contributor is likely to be 'chance' variation in how much history was measured for a particle, from iteration to iteration). Even with 32-bit precision representation, only those particles originating near the downstream wall, or in the vortex, were affected.

A likely reason for the insensitivity of results comes from consideration of the relationship between time, and stress contributions from the different time constants used to represent the memory function. Luo and Tanner [22] demonstrated that different time constants contribute most strongly to the overall stress at different deformation rates (an approximate inverse relationship is notable between the deformation rate and the 'dominant' time constants). Figure 15 shows how different time constants contribute to the total uniaxial elongational viscosity at different elongational rates (for model CR2 at the simulation temperature of 160°C). The deformation rates in contraction flow with an apparent shear rate of $64s^{-1}$ can be expected to be predominantly in the range 10^0 to 10^2 s^{-1}; from Figure 15 the greatest contributions to stress in this deformation rate range come from the time constants of 7.01×10^{-2} s, 7.01×10^{-1} s, and 7.01×10^{0} s. With 64-bit precision computation, the tracking time had normally exceeded 1000 seconds if the determinant limit was reached (with 'standard' integration); this time represents many multiples of the 'dominant' time constants, and is sufficient for accurate computation of stress contributions from all time constants up to 70.1 seconds. With 32-bit precision, the comparable figure for tracking time was around 100 seconds, which is sufficient to integrate all of the 'dominant' time constants accurately, with significant error expected in only the two longest time constants (the contributions from these time constants can be seen to be much lower than contributions from the dominant time constants at the characteristic deformation rates). This explains why the results obtained using 64-bit precision are very insensitive to the changes in the method used to compute **F** – all stress was well 'resolved', except for the stress due to the longest

time constant of 701 s, and this time constant is seen to contribute a very small fraction of overall stress for deformations around 10^0 to 10^2 s^{-1}. With 32-bit computation all time constants except the longest two are well-resolved; however these two time constants contribute very much less than the 'dominant' time constants (at the characteristic deformation rates of the flow), and the main features of the flow are captured with good accuracy, although with reduced convergence.

5. Discussion and Conclusions

The Molecular Stress Function Model with Convective Constraint Release is clearly a very significant step in rheological modelling. Within the confines of only two adjustable parameters, the steady-state shear viscosity, first normal stress difference, and both planar and uniaxial transient elongational data may be fitted for a strain-hardening polymer melt. The derivation from energy-balance considerations is based upon first principle physics, with a small number of assumptions. The two dissipative functions $g_1(\mathbf{S}, \mathbf{A_1})$ and $g_2(\mathbf{S}, \mathbf{A_1}, \mathbf{A_2})$ effectively isolate rotational and elongational effects, and give almost complete independence to the control of energy storage in purely elongational or purely shearing flow.

Upon application to a complex flow, via a finite element simulation, it was found that the vortex opening angles were lower than expected. The 5.75:1 axisymmetric contraction data from White and Kondo [29], showed clearly larger opening angles. The modification in Eq.12 aims to partially isolate the large values of f^2 caused by elongational flow, from the rotational content of the flow. As shown, the modification fits the experimental opening angle data much better than the original, with an equally good fit to the viscometric data. Application to a planar contraction flow showed that the modification gives much larger peak opening angles for such flows, in keeping with opening angles seen in experiment (e.g. [38]).

In simulation, the relative orientation tensor $\mathbf{S}(t'',t')$ is needed to allow the stretch $f^2(t,t')$ to be computed forwards to the current time, t, from each time t', in the past. The method given ensures that computation of the deformation tensor need only be performed once, using Eq.14; relative deformation gradients between any two intermediate times can then be computed by a (simple and fast) matrix-multiplication. The relative orientation tensor can be computed from the deformation gradient tensor either by direct integration, or by use of Currie's approximation. Accurate computation of the stress is significantly more 'involved' than KBKZ-type stresses. As with KBKZ type models, time steps need to be moderated for both accurate positional tracking, and accurate integration of the memory-function terms. To accurately trace f^2 it was found necessary to further moderate time-steps to ensure that the strain-rate history was well-resolved; if this is neglected both accuracy and convergence suffer significantly. The computation of f^2 is prohibitively expensive if calculated at each stored point. The method described for linear interpolation of f^2 between direct computation points, coupled to the adaptive computation point selection method, reduced our solution-time by a factor of over 20.

The linear combination of $g_1(\mathbf{S}, \mathbf{A_1})$ and $g_2(\mathbf{S}, \mathbf{A_1}, \mathbf{A_2})$ in the convective constraint release mechanism was originally chosen as the "simplest ansatz", a 'minimum assumption' continuation that agreed well with experimental results from viscometric rheological data. This work shows evidence from comparison of experimental vortex opening angle measurements and simulations of complex flows that the linear combination causes reduced opening angles, through interaction between the rotational component of flow and the large stretches that are caused principally by contraction (through $g_2(\mathbf{S}, \mathbf{A_1}, \mathbf{A_2})$). The modification to the constraint release term, shown in Eq.12, reduces this interaction, giving greatly increased opening angles that are quantitatively closer to the data of White and Kondo and, at least qualitatively, closer to the large opening angles seen for planar contraction flows. It is of interest that two models that give equally good fits to the available viscometric rheological data, behave significantly differently in a complex flow containing different modes of deformation. The implication for constitutive models is that evaluation against mixed deformation mode flow data is desirable in addition to evaluation against viscometric measurements.

The study of the effect of finite precision on computation of the deformation gradient tensor, **F**, produced some interesting results. The method to compute the tensor by direct integration was found to maintain unity determinant until a point *approaching* that at which rounding errors in 64-bit representation would be expected to make the determinant alter from unity (judged by a 'condition number'); the use of finer integration time-steps gave no clear increase. A method that should (mathematically) 'force' the determinant to unity was found to fail, as expected, at only slightly higher values of the condition number. The results showed considerable insensitivity to changes in the computation method of **F**, even when the representation precision was reduced to 32-bit. Consideration of the dominant time constants in the flow leads to a likely reason for the insensitivity.

References

[1] Wagner M.H., A constitutive analysis of uniaxial elongational flow data of low-density polyethylene melt , J.Non-Newt.Fluid Mech., 4 (1978), 39.

[2] A.C. Papanastasiou, L.E. Scriven and C.W. Macosko., An Integral Constitutive Equation for Mixed Flows: Viscoelastic Characterization ,J. Rheol., 27 (1983), 387.

[3] S. Dupont and M.J. Crochet, The vortex growth of a K.B.K.Z. fluid in an abrupt contraction , J.Non-Newt.Fluid Mech., 29 (1988), 81.

[4] X.-L. Luo and R. I. Tanner, Finite element simulation of long and short die extrusion experiments using integral models, Int. J. Num. Meth. Eng., 25 (1988), 9.

[5] P. Olley, An adaptation of the separable KBKZ equation for comparable response in planar and axisymmetric flow , J. Non-Newt. Fluid Mech., 95 (2000), 35.

[6] E. Mitsoulis, M. Schwetz, and H. Munstedt, Entry flow of LDPE melts in a planar contraction, J. non-Newt. Fluid Mech., 111 (2003), 41.

[7] M.H. Wagner and J. Schaeffer, Nonlinear strain measures for general biaxial extension of polymer melts,J. Rheol., 36 (1992), 1.

[8] M.H. Wagner and J. Schaeffer, Assessment of nonlinear strain measures for extensional and shearing flows of polymer melts, J., Rheol. Acta, 33 (1994), 506.

[9] M.H. Wagner, P. Ehrecke, P. Hachmann, and J. Meissner, A constitutive analysis of uniaxial, equibiaxial and planar extension of a commercial linear high-density polyethylene melt J. Rheol., 42 (1998), 621.
[10] M.H. Wagner, H. Bastian, P. Hachmann, J. Meissner, S. Kurzbeck, H. Munstedt, and F. Langouche, The strain-hardening behaviour of linear and long-chain branched polyolefin melts in extensional flows, Rheol. Acta , 39 (2000), 97.
[11] P. Olley, A study of the quadratic molecular stress function constitutive model in simulation, J. non-Newt. Fluid Mech., 125 (2005), 171.
[12] M.H. Wagner, P. Rubio, and H. Bastian, The molecular stress function model for polydisperse polymer melts with dissipative convective constraint release J. Rheol, 45 (2001), 1387.
[13] G. Marrucci, Dynamics of entanglements: A nonlinear model consistent with the Cox-Merz rule , J. non-Newt. Fluid Mech., 62 (1996), 279.
[14] T.C.B McLeish, R.G. Larson, Molecular constitutive equations for a class of branched polymers: The pom-pom polymer ,J. Rheol. 42 (1998), 81.
[15] S.T. Milner, T.C.B. McLeish, A.E. Likhtman, Microscopic theory of convective constraint release , J.Rheol., 45 (2001), 539.
[16] R.G. Larson, T. Sridhar, L.G. Leal, G.H. McKinley, A.E. Likhtman, T.C.B. McLeish, Definitions of entanglement spacing and time constants in the tube model, J. Rheol. 47 (2003), 809
[17] G. Ianniruberto and G. Marrucci, A simple constitutive equation for entangled polymer with chain stretch, J. Rheol., 45 (2001), 1305.
[18] G. Ianniruberto and G. Marrucci, A multi-mode CCR for entangled polymers with chain stretch, J. non-Newt. Fluid Mech., 102 (2002), 383.
[19] P. Wapperom, R. Keunings, G. Ianniruberto, Prediction of rheometrical and complex flows of entangled polymers using the double-convection-reptation model with chain stretch, J. Rheol., 47 (2003), 247.
[20] C.B.B Arjen, A.M. Grillet, G.W.M. Peters, F.P.T. Baaijens, Viscoelastic analysis of complex polymer melt flows using the eXtended Pom–Pom model , J. Non Newt. Fluid Mech., 108 (2002), 301.
[21] W.M.H. Verbeeten, G.W.M. Peters, F.P.T. Baaijens, Numerical simulations of the planar contraction flow for a polyethylene melt using the XPP model , J. Non Newt. Fluid Mech., 117 (2004), 73.
[22] X.-L. Luo, R.I. Tanner, A streamline element scheme for solving viscoelastic flow problems part II: Integral constitutive models, J. Non-Newt. Fluid Mech., 22 (1986), 61.
[23] X.-L Luo and E. Mitsoulis, A numerical study of the effect of elongational viscosity on vortex growth in contraction flows of polyethylene melts , J. Rheol., 34 (1990), 309.
[24] H.J. Park, D.G. Kiriakidis, E. Mitsoulis, Birefringence studies in die flows of an HDPE melt, J. Rheol. 36 (1992), 1563.
[25] P. Wapperom and R. Keunings, Numerical Simulation of branched polymer melts in transient complex flow using pom-pom models, J. non-Newt. Fluid Mech., 97 (2001), 267.
[26] E.A.J.F Peters, M.A. Hulsen, B.H.A.A. van den Brule, Instationary Eulerian viscoelastic flow simulations using time seperable Rivlin-Sawyers constitutive equations, J. non-Newt. Fluid Mech., 89 (2000), 209.
[27] H.K. Rasmussen, Lagrangian viscoelastic flow computations using the Rivlin-Sawyers constitutive model, J. non-Newt. Fluid Mech., 92 (2000), 227.

[28] H.K. Rasmussen, Lagrangian viscoelastic flow computations using a generalised molecular stress function model, J. non-Newt. Fluid Mech., 106 (2002), 107.
[29] J.L. White, A. Kondo, Flow patterns in polyethylene and polystyrene melts during extrusion through a die entry region: measurement and interpretation, J. non-Newt. Fluid Mech., 3 (1977), 41.
[30] M.H. Wagner, M. Yamaguchi, M. Takahashi, Quantitative assessment of strain hardening of low-density polyethylene melts by the molecular stress function model, J. Rheol., 47 (2003), 779.
[31] M.H. Wagner, J. Hepperle, H. Munstedt, Relating rheology and molecular structure of model branched polystyrene melts by molecular stress function theory, J. Rheol., 48 (2004), 489.
[32] J.M. Laun, Description of the non-linear shear behaviour of a low density polyethylene melt by means of an experimentally determined strain dependent memory function, Rheol. Acta., 17 (1978), 1.
[33] J.M. Laun, H. Munstedt, Elongational behaviour of a low density polyethylene melt, Rheol. Acta., 17 (1978), 415
[34] H.M. Laun H. Schuch, J. Rheology, Transient elongational viscosities and drawability of polymer melts, 33(1) (1989), 119.
[35] J. Meissner, Basic parameters, melt rheology, processing and end use properties of three similar low density polyethylene samples, Pure Appl. Chem., 42 (1975), 553-612
[36] P.K. Currie, Constitutive equations for polymer melts predicted by the Doi-Edwards and Curtiss-Bird kinetic theory models, J. non-Newt. Fluid Mech., 11 (1982), 53.
[37] M. Viriyayuthakon, B. Caswell, Finite element simulation of viscoelastic flow, J. non-Newt. Fluid Mech., 6 (1980), 245.
[38] M.T. Martyn, C. Nakason, P.D. Coates, Flow visualisation of polymer melts in abrupt contraction extrusion dies: quantification of melt recirculation and flow patterns, J. non-Newt. Fluid Mech., 91 (2000), 109.

Tables

	Vortex Intensity (%)	Opening Angle (degrees)	Correction Pressure
"standard" integration of **F** $\left(\Delta t_I \, g_{\max} \leq 1/5\right)$	6.64	50.4	7.38
finer integration of **F** $\left(\Delta t_I \, g_{\max} \leq 1/50\right)$	6.61	50.4	7.38
det(**F**)=1, enforced after standard integration	6.61	50.3	7.38
F computed to 32-bit precision	6.58	50.3	7.41

Table 1 Comparison of results obtained using different approaches to computing the deformation gradient tensor, **F**.

Appendix 1 Derivation of a condition number that relates rounding errors due to finite precision to the expected error in determinant

The expected unit determinant of the deformation gradient tensor, **F**, can be lost at high deformations, due to finite precision of representation. The following deduces a condition number that gives a measure of the expected error. The particular case analysed is for axisymmetric flow.

Consider a deformation gradient tensor, **F**, with all components correct to *infinite* precision, and a unit determinant:

$$\mathbf{F} = \begin{bmatrix} F_{rr} & F_{rx} & 0 \\ F_{xr} & F_{xx} & 0 \\ 0 & 0 & F_{\theta\theta} \end{bmatrix}.$$

As the determinant is unity, then

$$\left(F_{rr}F_{xx} - F_{rx}F_{xr}\right)F_{\theta\theta} = 1.$$

Consider now that one of the diagonal terms, (e.g. F_{xx}) is rounded up or down due to using a finite precision of N decimal digits. Taking the case of rounding down, F_{xx} is changed to F'_{xx} where $F'_{xx} = F_{xx} - \Delta$, and where $\Delta \sim \frac{F_{xx}}{10^N}$.

The new determinant is given by:

$$\left(F_{rr}F'_{xx} - F_{rx}F_{xr}\right)F_{\theta\theta}.$$

Substituting in the value for F'_{xx} gives a determinant of:

$$\left(F_{rr}\left(F_{xx} - \Delta\right) - F_{rx}F_{xr}\right)F_{\theta\theta},$$

which is equal to

$$\left(F_{rr}F_{xx} - F_{rx}F_{xr}\right)F_{\theta\theta} - \Delta F_{rr}F_{\theta\theta}.$$

The error in the determinant is thus $-\Delta F_{rr}F_{\theta\theta}$, but as $\Delta \sim F_{xx}/10^N$ then the error in the determinant is of the order of

$$\frac{F_{rr}\,F_{xx}\,F_{\theta\theta}}{10^N}.$$

The same result is found when the rounding of F_{rr}, or $F_{\theta\theta}$ is considered. Accounting for F_{rx} and F_{xr} in a similar manner gives an total expected error in the determinant of the order of

$$\frac{\frac{1}{2}\left(\left|F_{rr}\,F_{xx}\,F_{\theta\theta}\right| + \left|F_{rx}F_{xr}F_{\theta\theta}\right|\right)}{10^N},$$

for calculations with N decimal digits. This suggests a useful 'condition number', C, where

$$C = \frac{1}{2}\left(\left|F_{rr}\,F_{xx}\,F_{\theta\theta}\right| + \left|F_{rx}F_{xr}F_{\theta\theta}\right|\right).$$

The corresponding condition number for planar flow is $\frac{1}{2}\left(\left|F_{11}F_{22}\right| + \left|F_{12}F_{21}\right|\right)$.

Appendix 2 Method to adjust the deformation gradient tensor, F, to have a determinant of unity

The method to adjust **F** to give unity determinant is as follows:
If the flow is axisymmetric, then $F_{\theta\theta}$ is altered to its analytical value given by $r(t')/r(t)$ where $r(t)$ is the distance from the centreline at the current time, t, and $r(t')$ is the distance from the centreline at the earlier time, t' (from ref. [22]). Physically this should guarantee that $F_{\theta\theta}$ is greater than zero (it did when tested on the 5.75:1 axisymmetric flow). Having performed this modification, the determinant of **F**, d, is calculated. **F** is then modified to be a 'unity determinant' deformation gradient tensor ($\hat{\mathbf{F}}$) using:

$$\hat{F}_{\theta\theta} = F_{\theta\theta},$$

$$\hat{F}_{rr} = F_{rr} \Big/ d^{\frac{1}{2}},$$

$$\hat{F}_{xx} = F_{xx} \Big/ d^{\frac{1}{2}},$$

$$\hat{F}_{rx} = F_{rx} \Big/ d^{\frac{1}{2}},$$

and $$\hat{F}_{xr} = F_{xr} \Big/ d^{\frac{1}{2}}.$$

The method alters values in proportion to their existing size; because the direct integration method used to compute **F** can maintain an accurate determinant until machine precision is approached, alterations will be very small until high deformation. After this point this method will forcibly maintain unity determinant (provided that the determinant has remained positive) until numerical precision is insufficient to represent the deformations with unity determinant.

List of Figures

Figure 14 Contours of Principal Stress Difference for three MSF based models in a 8:1 ratio planar contraction flow. Apparent shear rate is 32 s^{-1}; contours are plotted at integer multiples of 35 kPa.

Figure 15 Spectrum decomposition of uniaxial elongational viscosity from the MSF model with convective constraint release (model CR2 with $a_1 = 0.012, a_2 = 0.55$) for IUPAC LDPE at 160°C. The six longest time constants are shown.

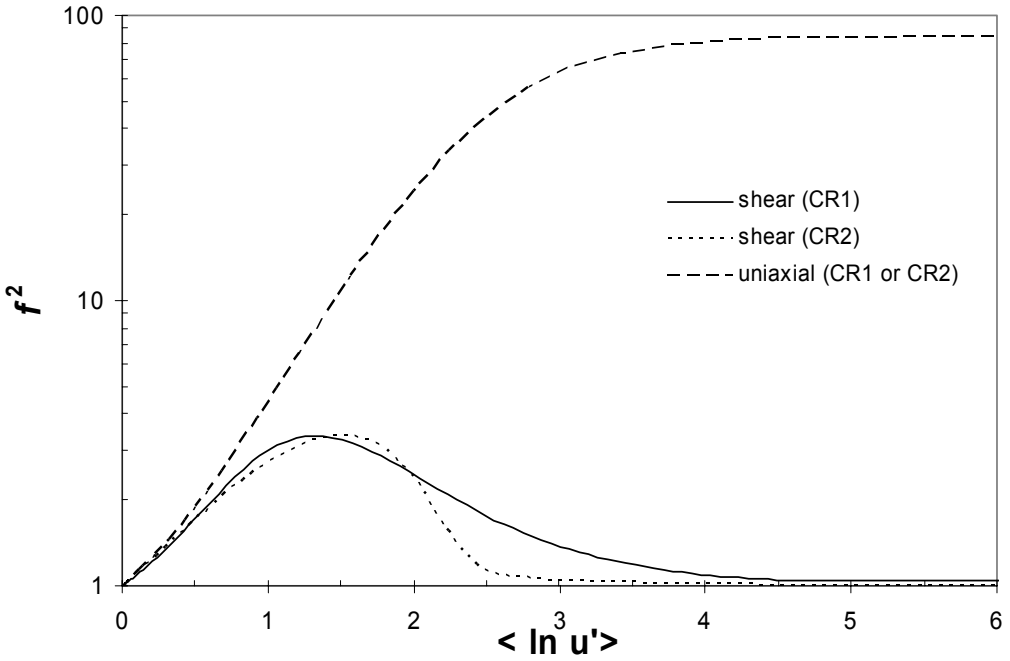

Figure 1 Variation of f^2 using different convective constraint release mechanisms in shear and uniaxial elongation. Model CR1 uses a_1=0.012, a_2=0.07; model CR2 uses a_1=0.012, a_2=0.55. Planar elongation gives identical curve to uniaxial elongation to graphical scale.

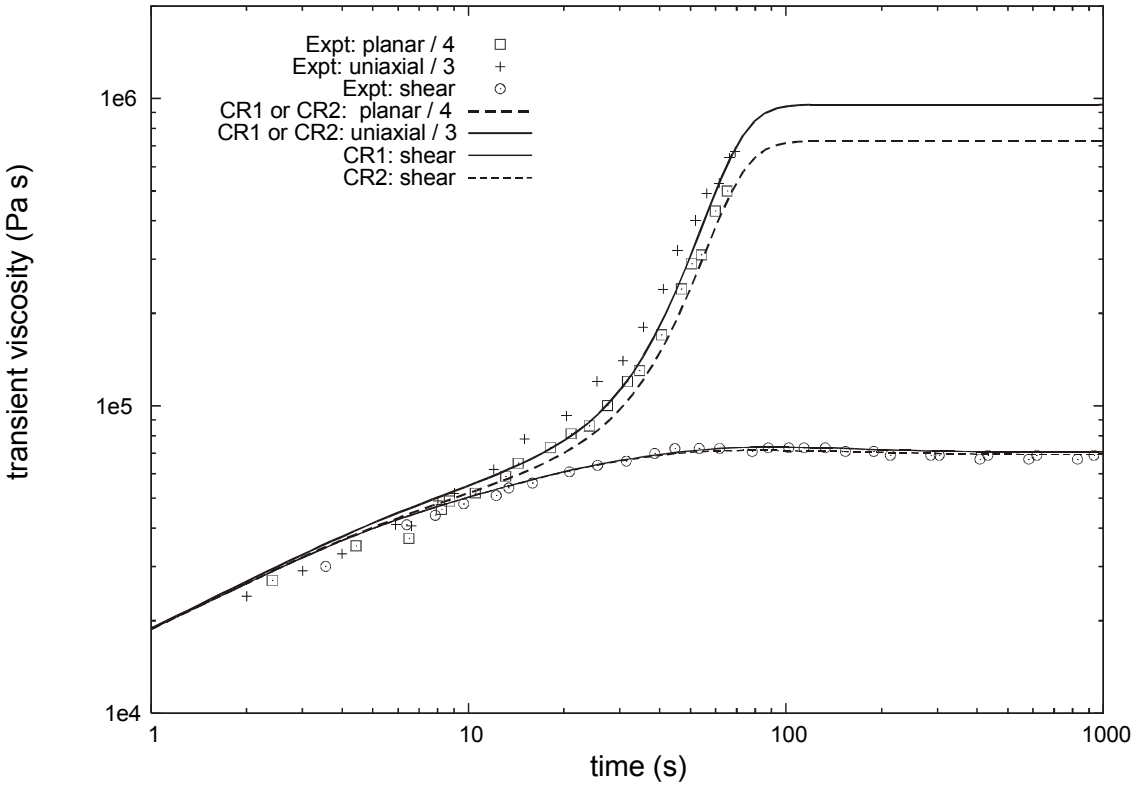

Figure 2 Comparison of transient experimental data for IUPAC LDPE at 125°C with predictions from the MSF model with convective constraint release (constraint release model CR1 with a_1=0.012, a_2=0.07, and CR2 with a_1=0.012, a_2=0.55)

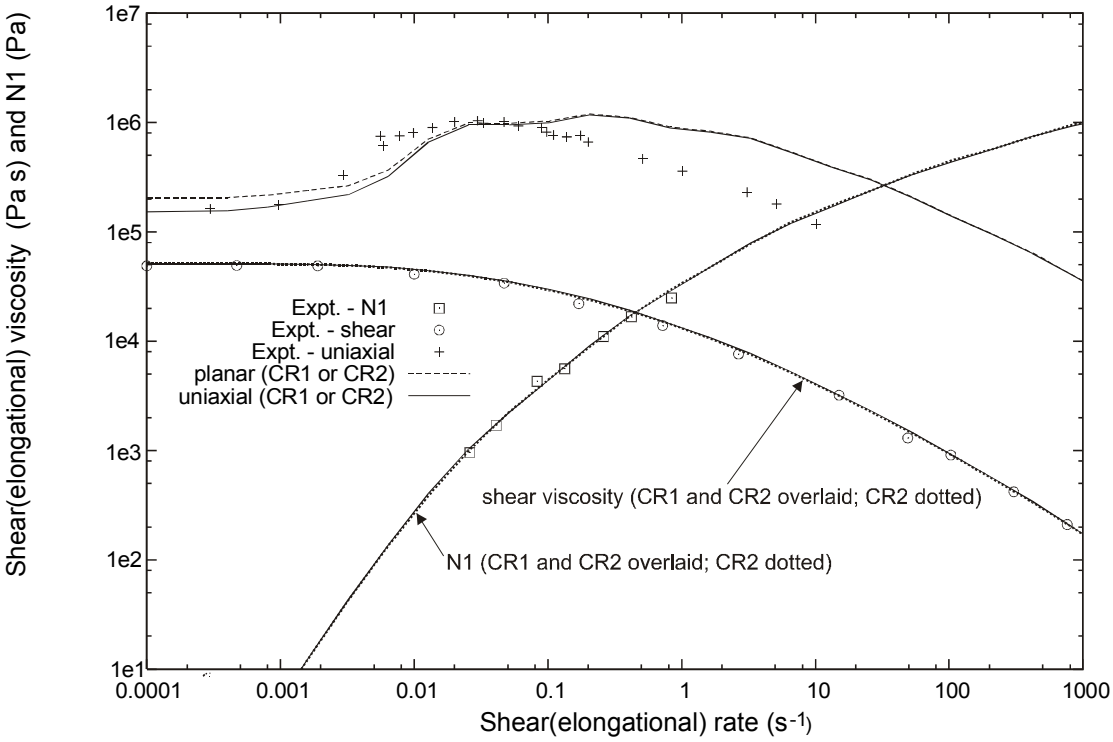

Figure 3 Comparison of steady-state experimental data for IUPAC LDPE at 150°C with predictions from the MSF model with convective constraint release (model CR1 with a_1=0.012, a_2=0.07 and model CR2 with a_1=0.012, a_2=0.55)

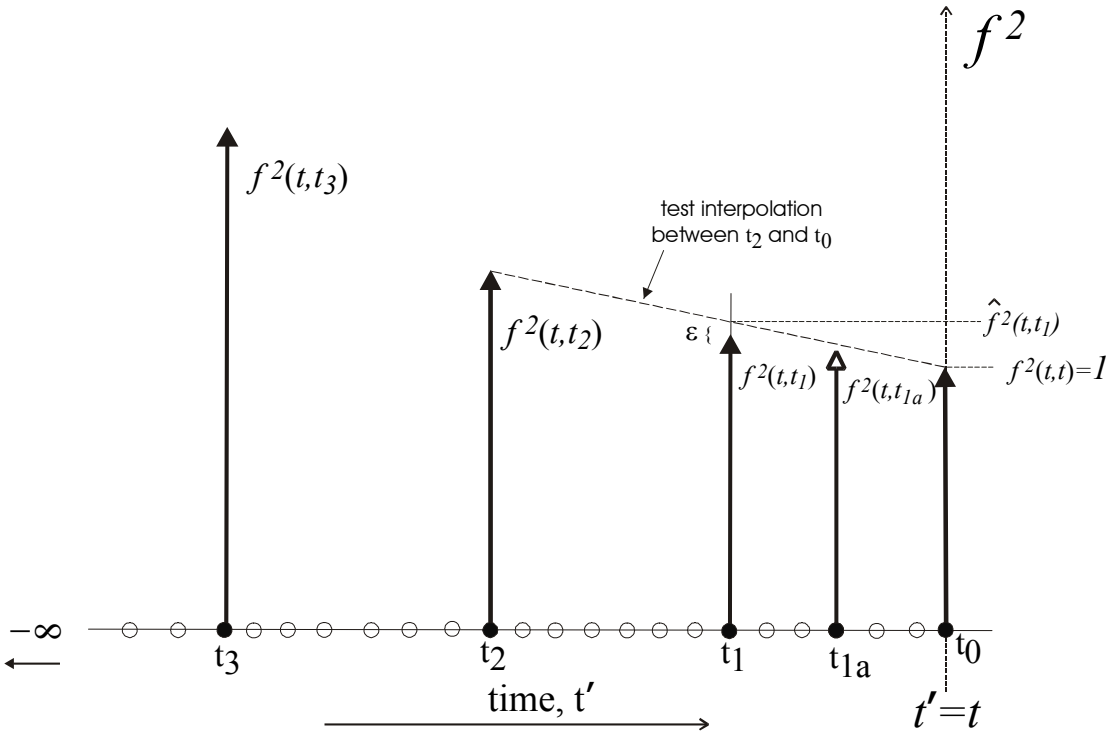

Figure 4 Test for adequate interpolation over the two intervals (initially) t_0 to t_2.

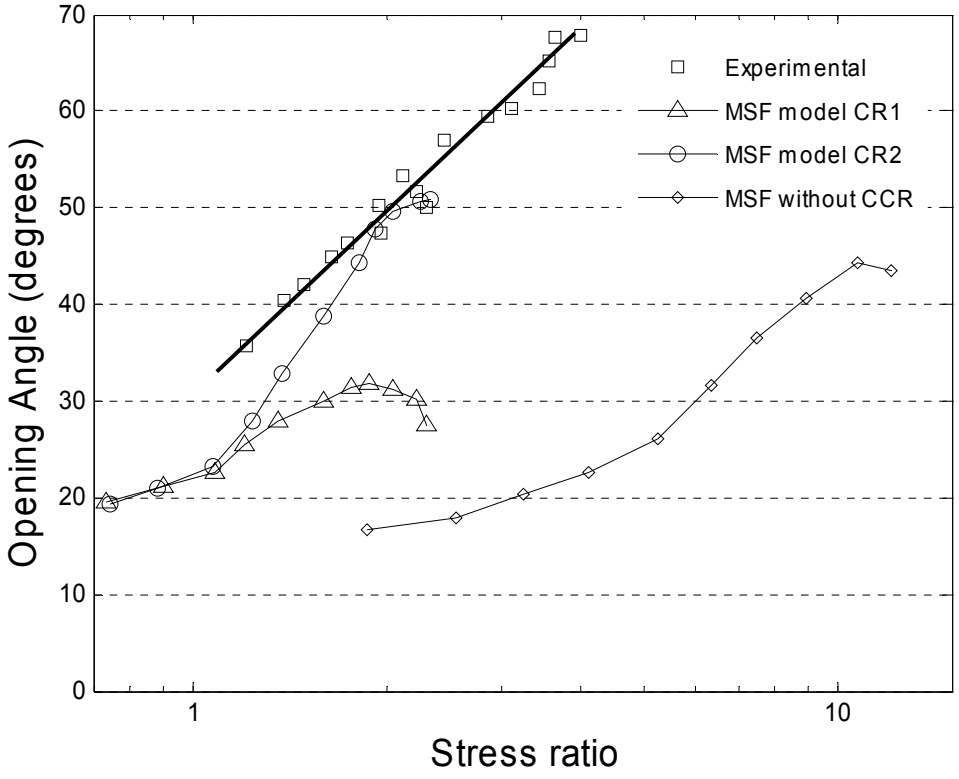

Figure 5 Comparison of experimentally measured opening angles from White and Kondo [29], and the opening angles obtained by three MSF based constitutive models in a 5.75:1 axisymmetric contraction flow of LDPE

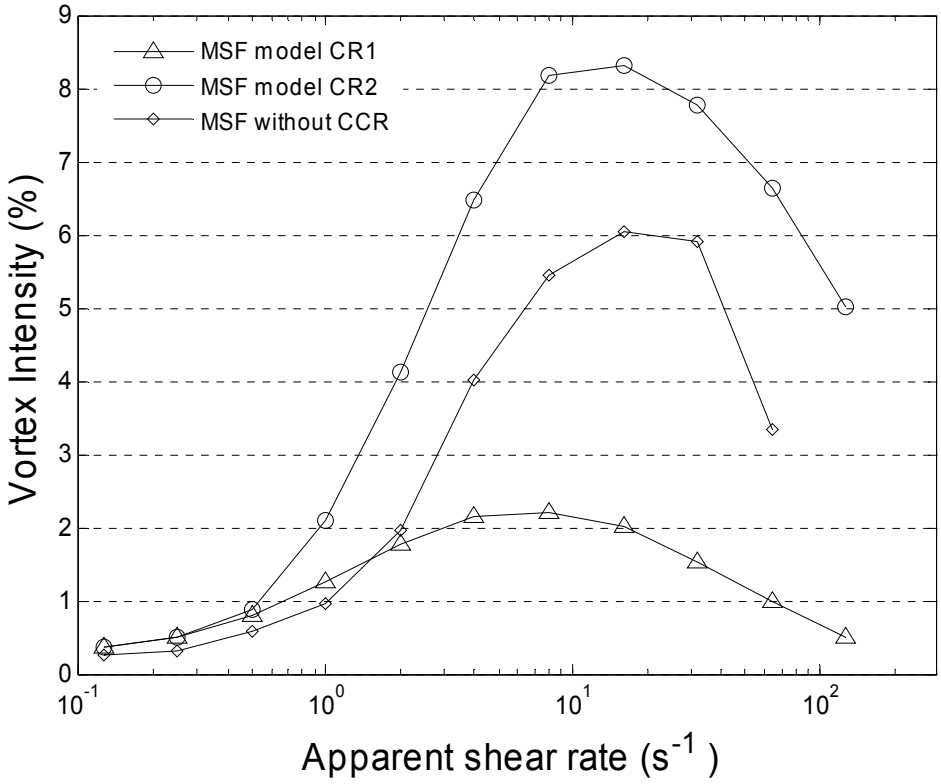

Figure 6 Comparison of the vortex intensity obtained by three MSF based constitutive models in a 5.75:1 axisymmetric contraction flow of LDPE

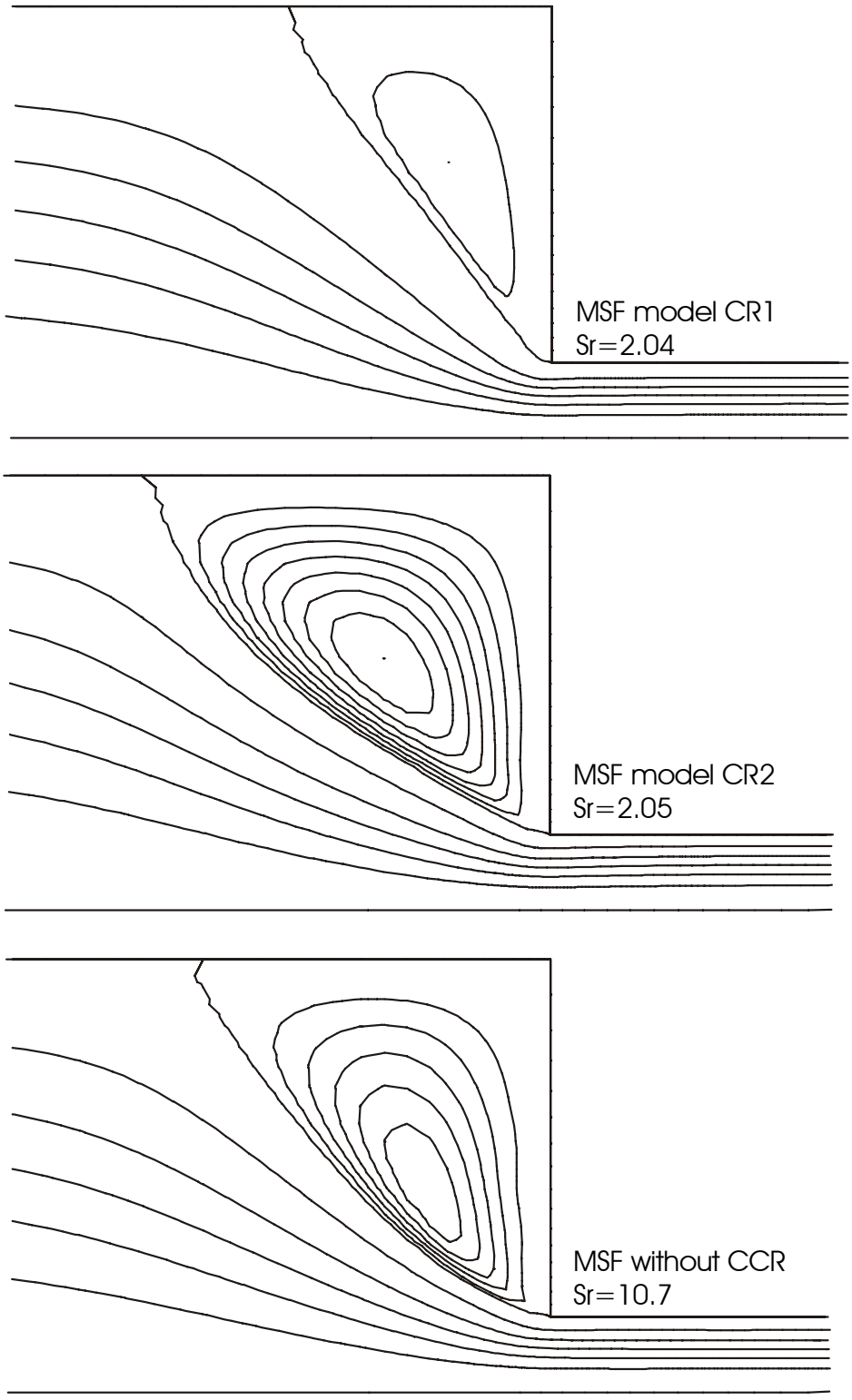

Figure 7 Contours of streamfunction in a 5.75:1 axisymmetric contraction at an apparent shear rate of $32s^{-1}$. Contours in the vortex are at integer multiples of 1% vortex intensity.

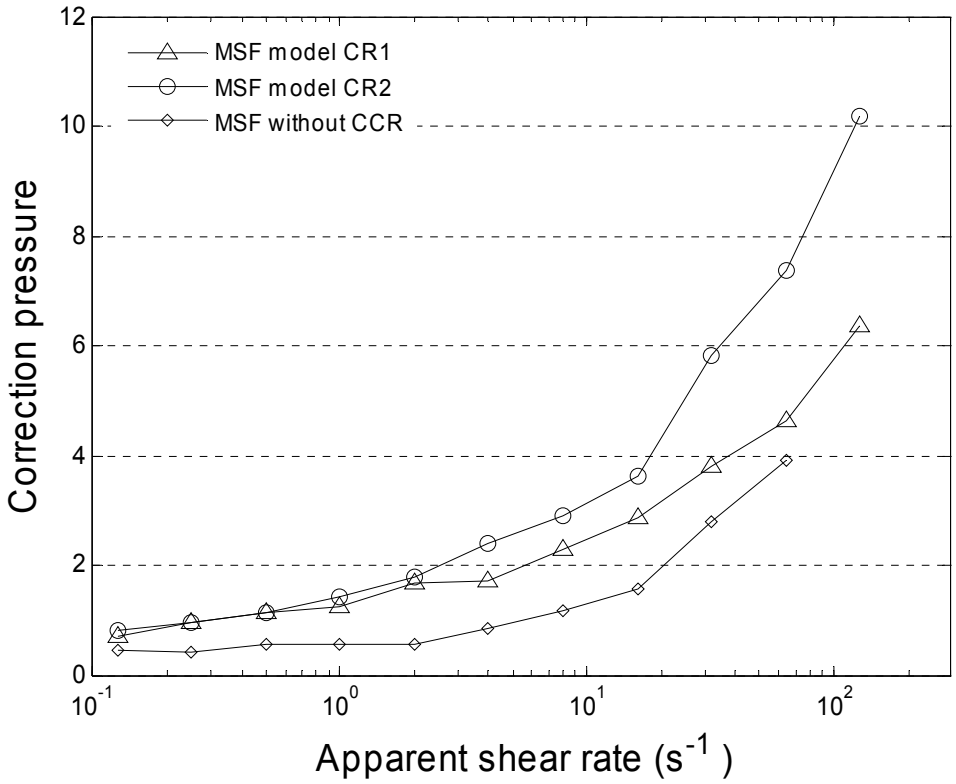

Figure 8 Comparison of the correction pressure obtained by three MSF based constitutive models in a 5.75:1 axisymmetric contraction flow of LDPE

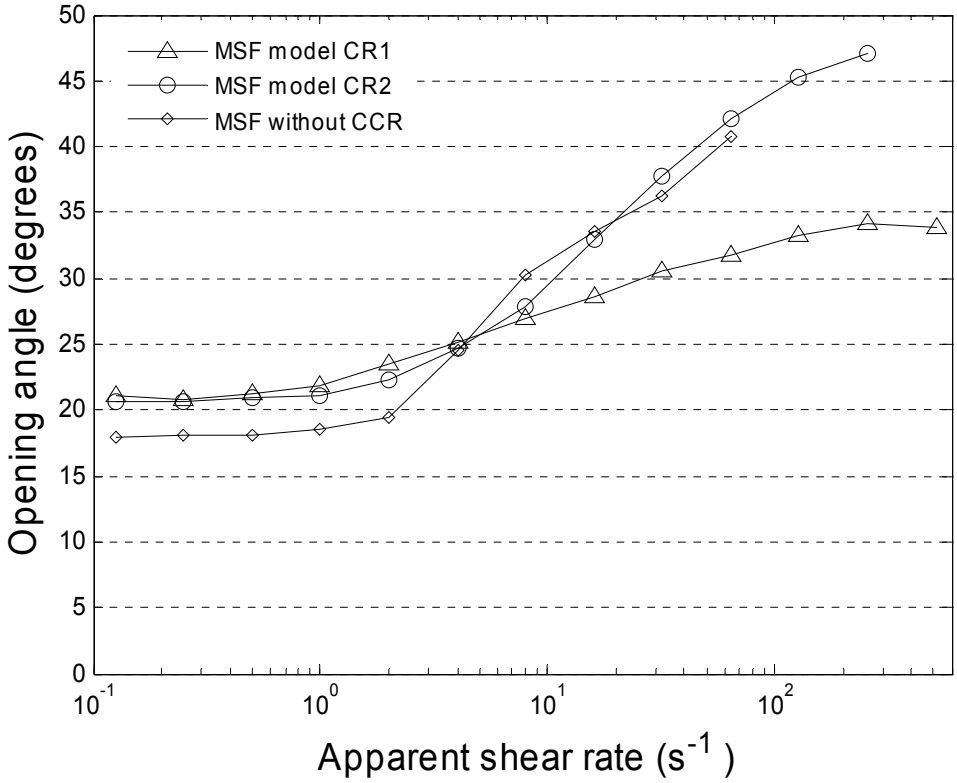

Figure 9 Comparison of the opening angle obtained by three MSF based constitutive models in a 8:1 planar contraction flow of LDPE

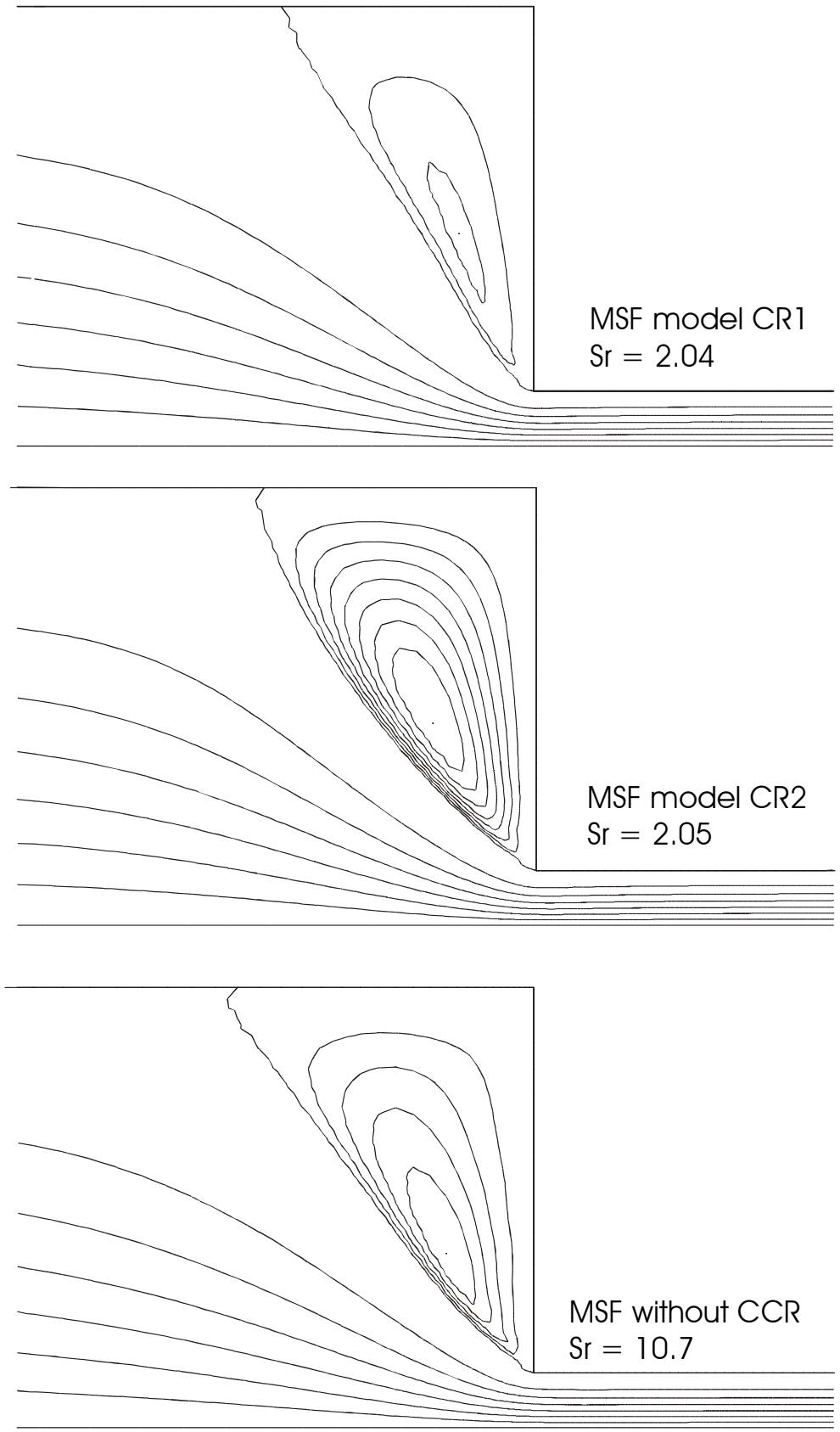

Figure 10 Contours of streamfunction in a 8:1 planar contraction at an apparent shear rate of $32s^{-1}$. Contours in the vortex are at integer multiples of 0.2% vortex intensity.

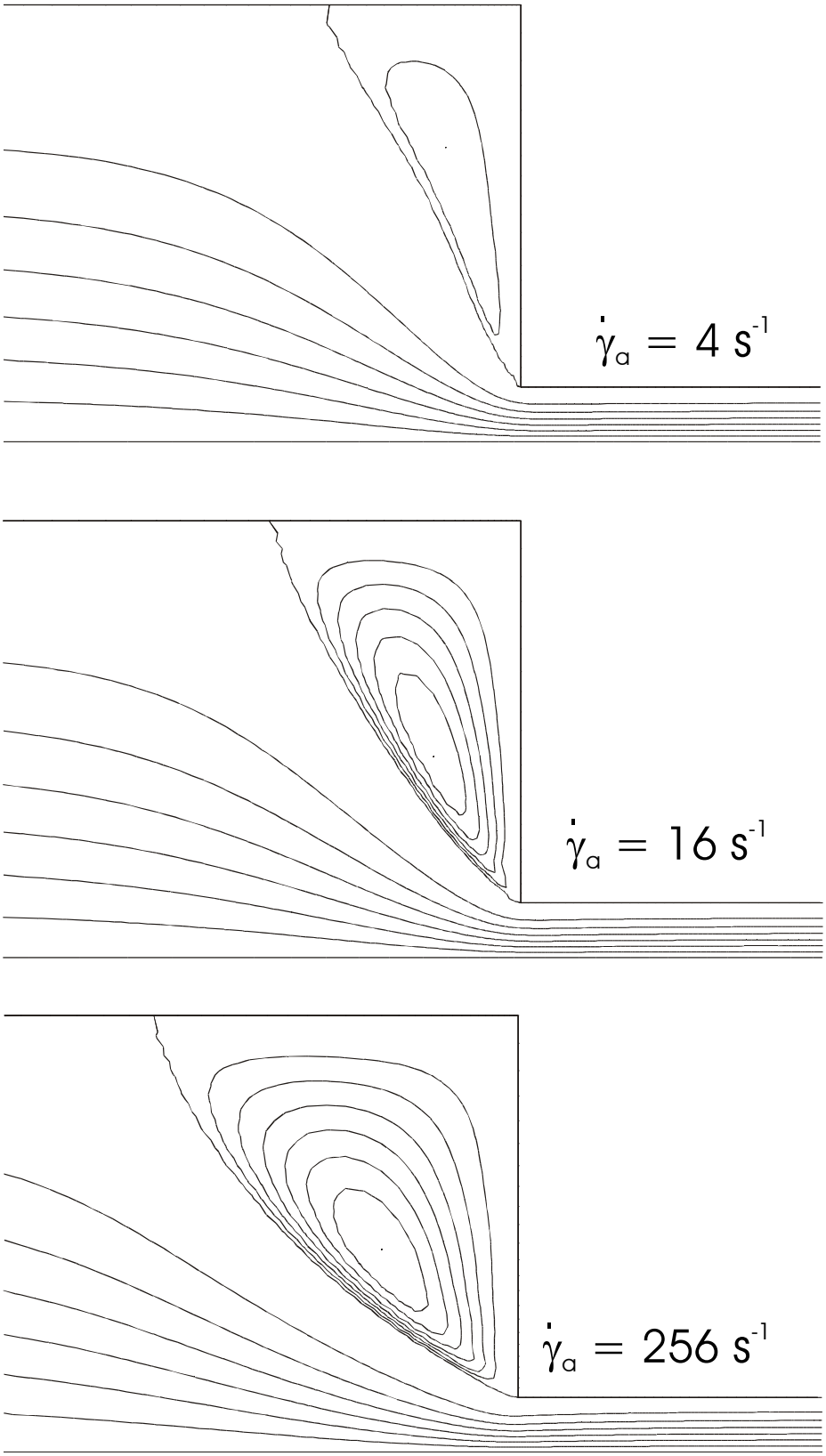

Figure 11 Contours of streamfunction in a 8:1 planar contraction for the MSF with convective constraint release mechanism CR2. Contours in the vortex are at integer multiples of 0.2% vortex intensity. The corresponding stress ratios, in order of increasing apparent shear rate, are 1.59, 1.88, and 2.44 .

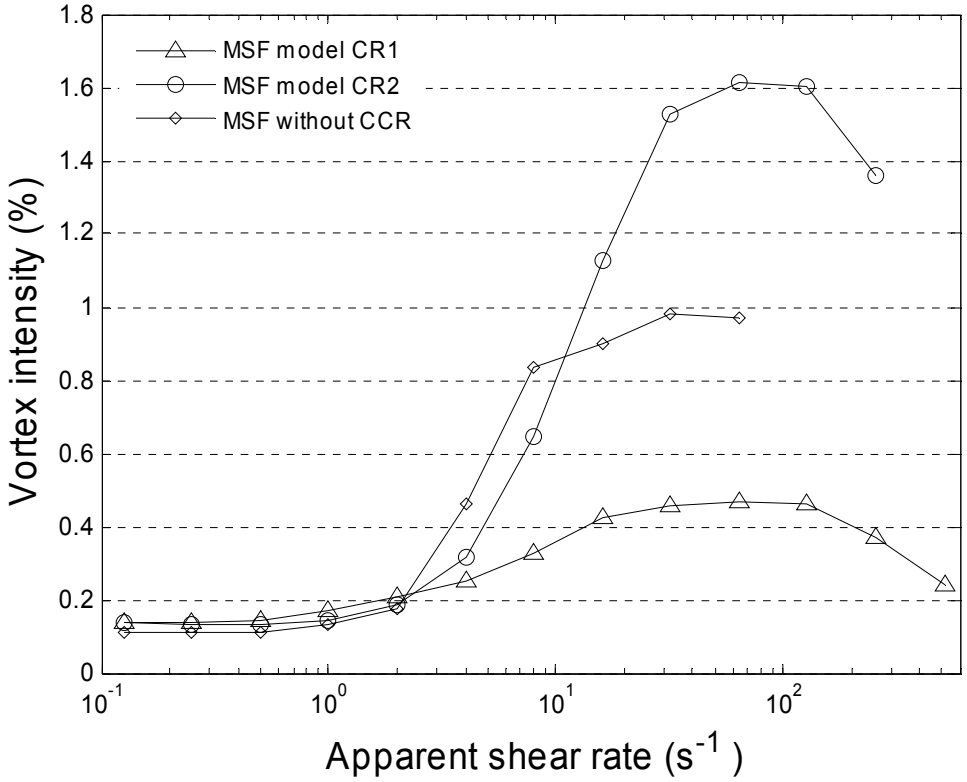

Figure 12 Comparison of the vortex intensity obtained by three MSF based constitutive models in a 8:1 planar contraction flow of LDPE

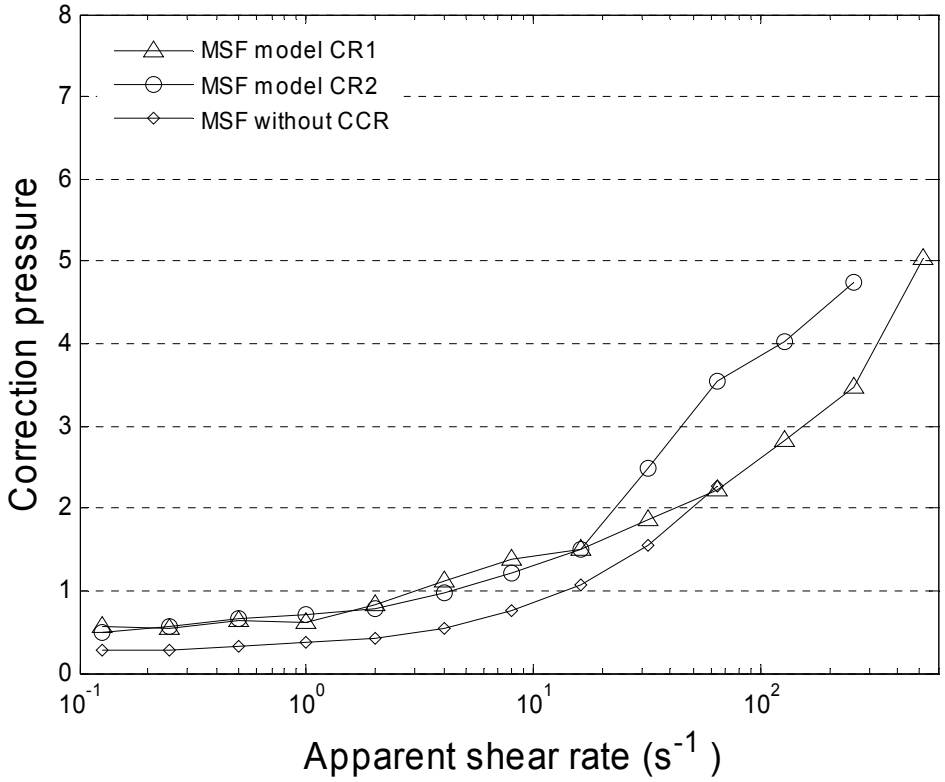

Figure 13 Comparison of the correction pressure obtained by three MSF based constitutive models in a 8:1 planar contraction flow of LDPE

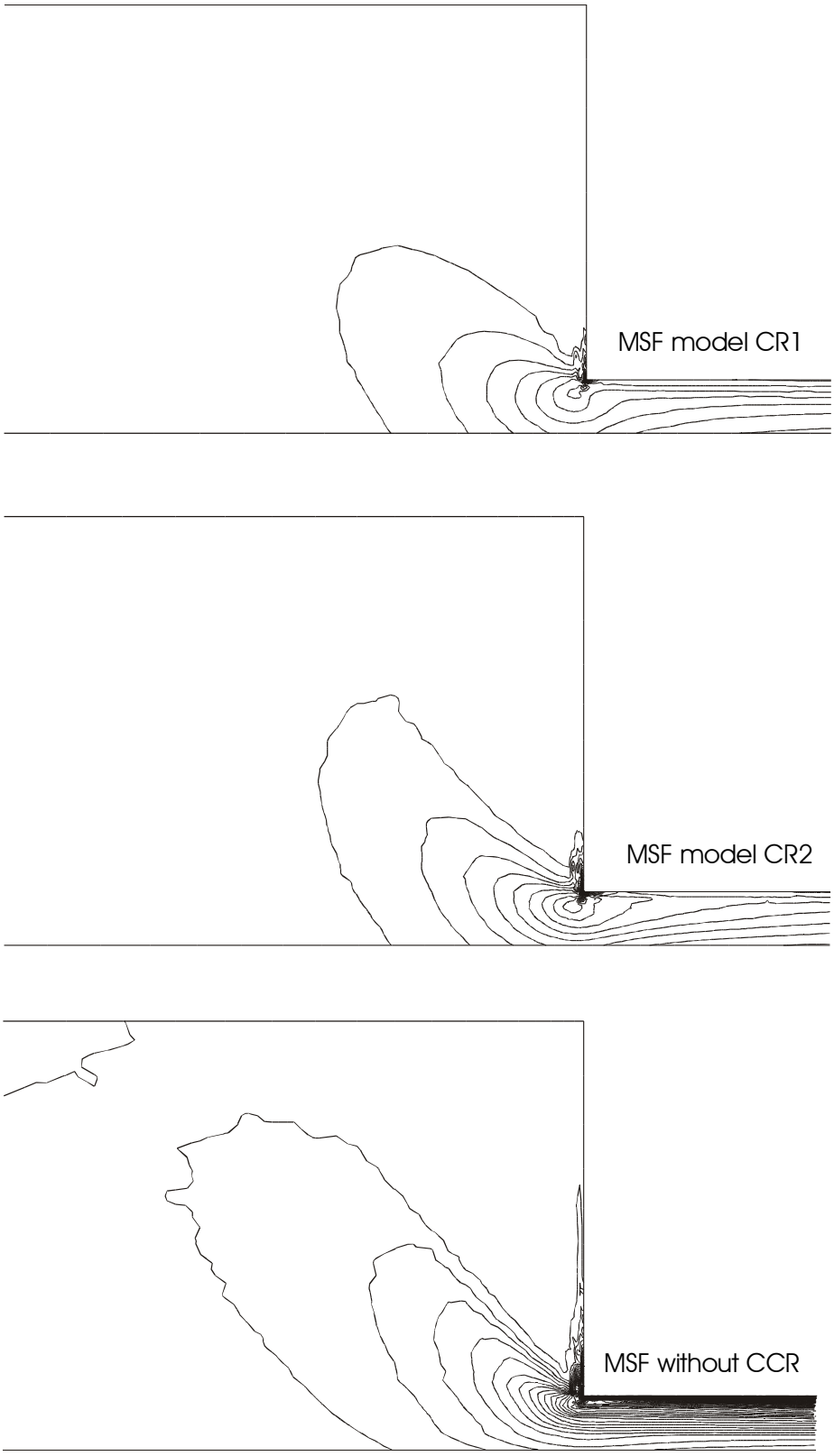

Figure 14 Contours of Principal Stress Difference for three MSF based models in a 8:1 ratio planar contraction flow. Apparent shear rate is 32 s^{-1}; contours are plotted at integer multiples of 35 kPa.

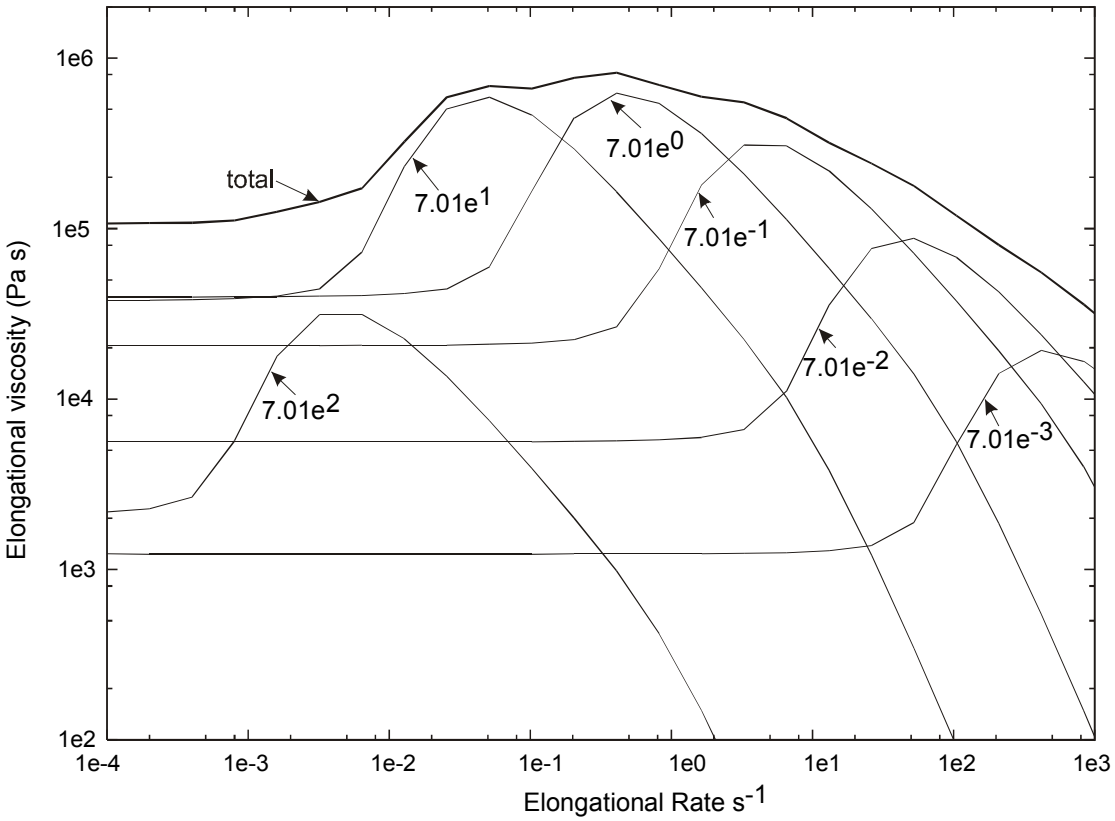

Figure 15 Spectrum decomposition of uniaxial elongational viscosity from the MSF model with convective constraint release (model CR2 with $a_1 = 0.012, a_2 = 0.55$) for IUPAC LDPE at 160°C. The six longest time constants are shown.